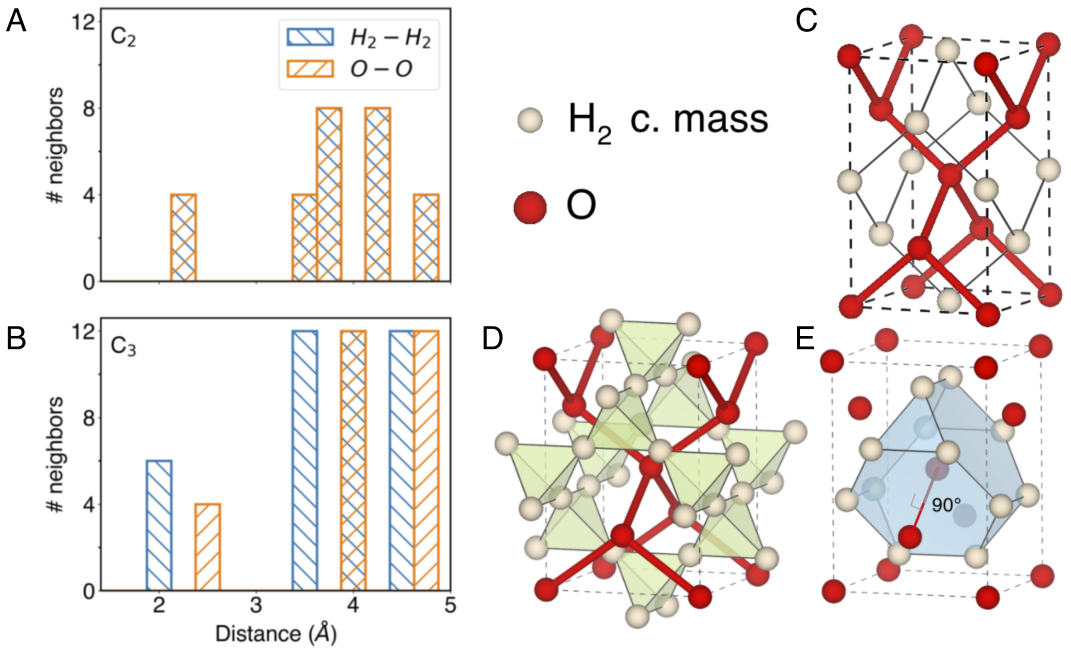

Fig. 4. Crystal structures of C_2 and C_3 highlighting the oxygen and H_2 sublattices. (*A* and *B*) Histograms of the number of neighboring O–O and H_2–H_2 as a function of distance in the C_2 and C_3 phase, respectively, at a pressure of 40 GPa. (*C*) Crystal structure of C_2. (*D* and *E*) Crystal structure of C_3. Oxygen atoms and H_2 centers of mass are shown as red and white spheres, respectively.

ice structures and account for the very high hydrogen density of this hydrate. While several gas hydrates were reported to have structural transitions at about 1–2 GPa (7, 8), hydrogen hydrate is only the second gas hydrate to show a phase transition above 10 GPa and to survive Megabar pressures. For methane hydrate, a structural transition from phase III (MH-III) to phase IV (MH-IV) is observed under compression to about 40 GPa at room temperature (36, 38). This is a transition between two different water sublattices for a constant methane-to-water molar ratio. Comparing the water frameworks, we can identify a common skeleton of all the filled ice structures showing remarkable high-pressure stability: the C_2 and C_3 phases and the methane hydrate phase MH-IV (36) share the ice I frame, either ice I*h* or ice I*c*, as shown in Fig. 5. The recurrence of the ice I network at high pressure is the result of an optimal compromise between the maximization of the hydrogen bond strength and a low efficiency-

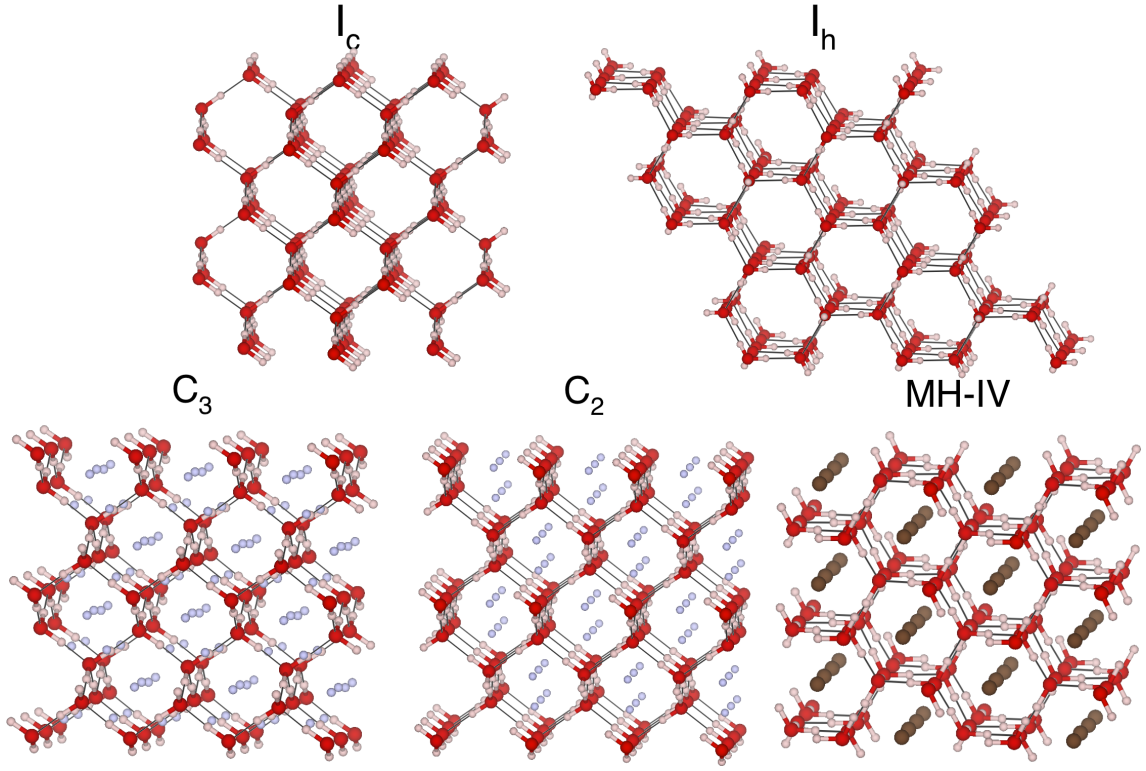

Fig. 5. Comparison between the crystal structures of the (low-pressure) water ice phases I*h* and I*c* and those of the related (high-pressure) phases C_2 and C_3 of hydrogen hydrate, and MH-IV of methane hydrate. Oxygen and hydrogen atoms of the water molecules are shown as large red and small pink spheres in a ball-and-stick model. The centers of mass of H_2 and CH_4 are shown as cyan and brown spheres, respectively. Hydrogen bonds are shown as black solid lines.

packed water structure—about 1/3 for both ice I*h* and I*c*—which thus retains the ability to host small molecules.

The high-pressure phase of methane hydrate (MH-IV) has been shown to survive to pressure up to 150 GPa at least (36); however, it is presently unclear whether it is thermodynamically stable or only metastable (see for example ref. 39). The volume of methane hydrate is indeed higher than that of the sum of its separated components (water ice and pure solid methane), in both phases MH-III and MH-IV. The comparison between the volume of methane hydrate (38) and of the components (31, 40) is reported in *SI Appendix*, Fig. S10. On the other hand, the hydrogen hydrate phase C_2 also has a larger volume than the sum of its separated pure components but C_3 is presently unique in being slightly denser than its constituent elements (Fig. 2*C*). According to our calculations, C_3 remains thermodynamically stable against decomposition up to 200 GPa at least (*SI Appendix*, Fig. S1). By contrast, the hydrates of argon, krypton, xenon, and carbon dioxide have all been reported to fully decompose upon compression to pressures of about 1 to 6 GPa (41, 42), and for nitrogen hydrate, a recent work reported no stable solid phases from 5 GPa to 140 GPa (43). Yet, it seems unlikely that methane and hydrogen hydrates are exceptions and future studies will be able to verify whether other small non-polar guests, such as for example, helium, neon, or dioxygen can form a similar structure with water at extreme pressures. It is possible that an entire class of filled ice I gas hydrates exists at pressures compatible with those encountered in the interior of large gaseous and icy planets of our solar system or Neptune-like exoplanets.

Materials and Methods

Experimental Details. Starting polycrystalline hydrogen hydrate samples having the clathrate sII structure were prepared by exposing H_2O ice (I*h*) to gas H_2 at 0.28 GPa for 20–30 min, following the method described in ref. 44. The ice was made of spheres with typical diameters of a few tens of micrometers. After preparation, the samples were recovered at ambient pressure and stored at liquid nitrogen temperature. For the high-pressure experiments, a small amount of sample was loaded at low temperature in a diamond anvil cell that was partially immersed in a liquid nitrogen bath. The loaded sample was then compressed to pressures of a few GPa before being warmed up to room temperature. This is a similar loading procedure to what we had previously done for methane hydrate (35, 36). This procedure inevitably produces a mixture of C_2 hydrogen hydrate and excess pure ice, because of the difference in molar ratios between the clathrate sII phase and the C_2 phase. Clathrate sII samples prepared following our method have a molar ratio H_2O:H_2 between 4 and 5, as we have verified by neutron diffraction in the past (44), and the C_2 phase is characterised by a molar ratio of 1. One sample was prepared directly in the DAC by loading room-temperature liquid H_2O and high-pressure H_2 at 0.14 GPa using a gas loading setup. This sample was measured by Raman spectroscopy and by XRD. Similarly to the cryo-loaded samples, it also formed hydrogen hydrate with the structure C_2 and after laser heating at 40 GPa, with the structure C_3. Some of the samples contained a small amount of pure N_2 and/or pure O_2, both of which can be easily identified from their respective vibron Raman peaks. Those must have been trapped in the sample chamber during cryo-loading and acted as a pressure-transmitting medium. Some of the samples did not contain N_2 or O_2 and an example of Raman spectrum for such a sample is reported in *SI Appendix*, Fig. S11. Culet diameters ranging between 100 and 300 μm for the diamond anvils were employed. Re-foil gaskets were used to contain the sample.

A Nd-YAG laser system (wavelength of 1.064 μm) was employed to heat the sample, using gold as the laser coupler. Angle-dispersive X-ray powder diffraction patterns were acquired at ID15b at ESRF (Grenoble, France) using a monochromatic X-ray beam (λ = 0.41 Å) and an Eiger 2 9M CdTe flat-panel detector, with a typical acquisition time of a few seconds. The beam spot size was 6×6 μm. The 2D diffraction patterns were treated to mask the Bragg peaks of the diamond anvils then integrated into one-dimensional patterns, and a smooth polynomial background was subtracted. Le Bail refinements were performed using FullProf. In the XRD measurements, pressure was determined using the equation of state of gold from ref. 45. Raman spectra were acquired using a commercial Horiba Jobin–Yvon LabRam HR800 Raman spectrometer in a backscattering geometry, equipped with a COBOLT SambaTM 1000-mW green laser. Acquisition time was typically of about a minute. A smooth background was subtracted from the Raman spectra before fitting the data and examples of fits for C_2 and C_3 at 50 and 75 GPa are reported in *SI Appendix*, Fig. S12. Reference spectra were recorded at each pressure from the gasket close to the sample chamber and particular care was taken to check the effect of the background subtraction on the fit results. In the Raman measurements, pressure was determined by the shift of the R1 ruby fluorescence line (46), from the edge of the stressed diamond signal (47) or from the vibron frequency of pure solid H_2 (34). All measurements were performed at room temperature.

Many sample loadings were performed for this study, as mentioned above, and Fig. 3 results from data merged together from different loadings. In *SI Appendix*, Fig. S13, we show Raman spectra and corresponding vibron frequencies for one single sample loading over the whole investigated pressure range, before and after laser heating. Several loaded samples were compressed and measured by Raman spectroscopy without performing laser heating, applying different compression rates to check whether the C_3 phase would form. Some indications of the possible formation of a small amount of C_3 at room temperature above 70 GPa have been observed in some of the Raman experiments (*SI Appendix*, Fig. S14) but this point requests further investigation. One sample containing the C_2 phase was decompressed and measured by Raman spectroscopy. The corresponding frequencies are reported in panel *A* of *SI Appendix*, Fig. S15, where it can be seen that the pressure dependence of the peak frequencies is the same upon compression and decompression. Furthermore, we observe that no major changes occur upon decompression in the relative peak intensities of C_2 hydrogen hydrate and of pure H_2, meaning that the partial decomposition of the hydrate is irreversible. We also decompressed the C_3 phase by Raman spectroscopy and observed it can be recovered down to at least 36 GPa at room temperature (*SI Appendix*, Fig. S15*B*). The stability of the C_3 phase under decompression is an important information in order to envisage the use of high-density hydrates as H_2 storage material and future studies will be able to check whether the C_3 phase can be recovered at ambient pressure and low temperature.

Simulation Methods. Crystal structure prediction was performed using evolutionary algorithm as implemented in the USPEX code (27, 28). The structures were relaxed using a five-step process with the Vienna ab initio simulation package (VASP) as a DFT code (48), employing the projector-augmented wave pseudopotentials with Perdew–Burke–Ernzerhof pseudopotentials provided with the package (49). Further details are provided in *SI Appendix*.

The C_2 and C_3 phases were simulated using Density Functional (Perturbation) Theory as implemented in Quantum ESPRESSO (50, 51), using Optimized Norm-Conserving Vanderbilt pseudopotentials (ONCV) (52) and optimized Becke88 van der Waals exchange-correlation functional (53–55). A cutoff of 90 Ry was employed on the plane waves' expansion, and the integration of the Brillouin zone was performed over a 4×4×4 grid in reciprocal space with fixed occupations. The vibrational zero-point energy was computed within the harmonic approximation over a 2×2×2 grid in reciprocal space, and integrated over a 8×8×8 grid using Fourier interpolation. We did not include temperature effects in our calculations of the thermodynamics properties. Proton-ordered configurations for the water molecules satisfying the Bernal–Fowler rules were obtained directly from the USPEX structural search calculations. Furthermore, consideration of the H_2 molecules as two individual atoms lowers the crystal symmetry in the simulations: The simulated structures are not cubic but tetragonal or orthorhombic (see *SI Appendix* for further details). Details of our C_2 and C_3 structures and unit cell dimensions as a function of pressure, calculated within DFT, are reported in *SI Appendix*, Table S2 and Fig. S8, respectively. For pure hydrogen and pure water, we used as references the (proton-ordered) structures of phase II (56) and ice VIII, respectively.

Anharmonicity and quantum nuclear effects were evaluated using the stochastic self-consistent harmonic approximation as implemented in the SSCHA

code (29, 30). The SSCHA minimizes the free energy $F[\hat{\rho}] = \langle H \rangle_{\hat{\rho}} - TS[\hat{\rho}]$ by optimizing a trial density matrix $\hat{\rho}$ constrained among solutions of an auxiliary harmonic Hamiltonian. The free energy minimization is performed using the second-order Newton method, with a stochastic sampling of the Born–Oppenheimer energy landscape at DFT level (30). The method allowed us to evaluate the strength of quantum and anharmonic effects in the frequencies of the hydrogen vibron compared to the harmonic approximation. This method has been reported as the most successful to compute the phase diagram and Raman and IR spectra of H_2 vibrons at high pressure (57–60). The interested reader can find further information on the specific details employed in the simulation of C_2 and C_3 in *SI Appendix* and additional details on the numerical implementation in ref. 29.

Data, Materials, and Software Availability. All study data are included in the article and/or *SI Appendix*.

ACKNOWLEDGMENTS. We acknowledge the European Synchrotron Radiation Facility for provision of synchrotron radiation facilities at the ID15B beam line under proposal number HC-5060 and assistance from M. Hanfland, D. Comboni, and G. Garbarino. Preliminary measurements for this project were carried out at the ID27 beam line, and we thank M. Mezouar and A. Pakhomova. We thank the ANR-23-CE30-0034 EXOTIC-ICE. We acknowledge funding through the Swiss National Fund (FNS) grant EXOTIC-ICES n 212889, PRIN 2022 NRBLPT, and from progetto di ateneo RM120172B8E7BC07. S.D.C. acknowledges computational resources from CINECA, proj. IsC90-HTS-TECH and IsC99-ACME-C, and the Vienna Scientific Cluster, proj. 71754 "TEST." L.M. acknowledges computational resources from CSCS, Piz Daint, under project s1192 and the grant Marie Sklodowska-Curie Actions Individual Fellowship (MSCA IF), project codename THERMOH. We thank Werner F. Kuhs, Andrzej Falenty, Dirk Wallacher, and Alain Polian for help during sample preparation and Lewis Conway for kindly sharing his code for structural analysis. S.D.C. thanks Guang-Rui Qian for the useful discussion.

Author affiliations: [a]Dipartimento di Fisica, Sapienza Università di Roma, 00185 Roma, Italy; [b]Centre for Science at Extreme Conditions and School of Physics and Astronomy, University of Edinburgh, EH9 3FD Edinburgh, United Kingdom; [c]Institut für Festkörperphysik, Technische Universität Wien, 1040 Wien, Austria; [d]Laboratory of Quantum Magnetism, Institute of Physics, École Polytechnique Fédérale de Lausanne, CH-1015 Lausanne, Switzerland; [e]Theory and Simulation of Materials, and National Centre for Computational Design and Discovery of Novel Materials, École Polytechnique Fédérale de Lausanne, 1015 Lausanne, Switzerland; [f]Consiglio Nazionale delle Ricerche, Istituto Nazionale di Ottica, CNR-INO, Sesto Fiorentino, 50019, Italy; [g]European Laboratory for Nonlinear Spectroscopy, LENS, Sesto Fiorentino (FI), 50019, Italy; and [h]Sorbonne Université, UMR CNRS 7590, Institut de Minéralogie, de Physique des Matériaux et de Cosmochimie, 75252 Paris, France

1. J. H. Waite *et al.*, Cassini finds molecular hydrogen in the Enceladus plume: Evidence for hydrothermal processes. *Science* **356**, 155–159 (2017).
2. A. Bouquet, O. Mousis, J. H. Waite, S. Picaud, Possible evidence for a methane source in Enceladus' ocean. *Geophys. Res. Lett.* **42**, 1334–1339 (2015).
3. A. Bouquet, O. Mousis, C. R. Glein, G. Danger, J. H. Waite, The role of clathrate formation in Europa's ocean composition. *Astrophys. J.* **885**, 14 (2019).
4. E. S. Kite, E. B. Ford, Habitability of exoplanet waterworlds. *Astrophys. J.* **864**, 75 (2018).
5. W. L. Mao *et al.*, Hydrogen clusters in clathrate hydrate. *Science* **297**, 2247–2249 (2002).
6. E. Sloan, C. Koh, *Clathrate Hydrates of Natural Gases* (CRC Press, ed. 3, 2008).
7. J. Loveday, E. Nelmes, High pressure hydrates. *J. Phys. Chem. Chem. Phys.* **10**, 937–950 (2008).
8. L. E. Bove, U. Ranieri, Salt- and gas-filled ices under planetary conditions. *Philos. Trans. R. Soc. A* **377**, 20180262 (2019).
9. M. E. Donnelly, P. Teeratchanan, C. L. Bull, A. Hermann, J. S. Loveday, Ostwald's rule of stages and metastable transitions in the hydrogen-water system at high pressure. *Phys. Chem. Chem. Phys.* **20**, 26853–26858 (2018).
10. D. M. Amos *et al.*, A chiral gas-hydrate structure common to the carbon dioxide-water and hydrogen-water systems. *J. Phys. Chem. Lett.* **8**, 4295–4299 (2017).
11. L. del Rosso, M. Celli, L. Ulivi, New porous water ice metastable at atmospheric pressure obtained by emptying a hydrogen-filled ice. *Nat. Commun.* **7**, 13394 (2016).
12. T. A. Strobel, M. Somayazulu, S. V. Sinogeikin, P. Dera, R. J. Hemley, Hydrogen-stuffed, quartz-like water ice. *J. Am. Chem. Soc.* **138**, 13786–13789 (2016).
13. W. L. Vos, L. W. Finger, R. J. Hemley, H. Kwang Mao, Novel H_2–H_2O clathrates at high pressures. *Phys. Rev. Lett.* **71**, 3150–3153 (1993).
14. Y. Wang *et al.*, Novel hydrogen clathrate hydrate. *Phys. Rev. Lett.* **125**, 255702 (2020).
15. C. G. Salzmann, Advances in the experimental exploration of water's phase diagram. *J. Chem. Phys.* **150**, 060901 (2019).
16. K. Komatsu, Neutrons meet ice polymorphs. *Crystallogr. Rev.* **28**, 224–297 (2022).
17. G. R. Qian, A. O. Lyakhov, Q. Zhu, A. R. Oganov, X. Dong, Novel hydrogen hydrate structures under pressure. *Sci. Rep.* **4**, 5606 (2014).
18. L. Hakim, K. Koga, H. Tanaka, Phase behavior of different forms of ice filled with hydrogen molecules. *Phys. Rev. Lett.* **104**, 115701 (2010).
19. J. Zhang, J. L. Kuo, T. Iitaka, First principles molecular dynamics study of filled ice hydrogen hydrate. *J. Chem. Phys.* **137**, 084505 (2012).
20. G. S. Smirnov, V. V. Stegailov, Toward determination of the new hydrogen hydrate clathrate structures. *J. Phys. Chem. Lett.* **4**, 3560–3564 (2013).
21. J. Košata, P. Merkl, P. Teeratchanan, A. Hermann, Stability of hydrogen hydrates from second-order Møller–Plesset perturbation theory. *J. Phys. Chem. Lett.* **9**, 5624–5629 (2018).
22. T. Ikeda, Simulating Raman spectra of hydrogen hydrates using first-principles path-integral ring-polymer molecular dynamics. *Chem. Phys. Lett.* **792**, 139416 (2022).
23. S. Machida, H. Hirai, T. Kawamura, Y. Yamamoto, T. Yagi, Raman spectra for hydrogen hydrate under high pressure: Intermolecular interactions in filled ice Ic structure. *J. Phys. Chem. Solids* **71**, 1324–1328 (2010).
24. H. Hirai *et al.*, Structural changes of filled ice Ic hydrogen hydrate under low temperatures and high pressures from 5 to 50 GPa. *J. Chem. Phys.* **137**, 074505 (2012).
25. S. I. Machida, H. Hirai, T. Kawamura, Y. Yamamoto, Y. Yagi, Isotopic effect and amorphization of deuterated hydrogen hydrate under high pressure. *Phys. Rev. B* **83**, 144101 (2011).
26. W. L. Mao, H. Kwang Mao, Hydrogen storage in molecular compounds. *Proc. Natl. Acad. Sci. U.S.A.* **101**, 708–710 (2004).
27. C. W. Glass, A. R. Oganov, N. Hansen, USPEX-evolutionary crystal structure prediction. *Comput. Phys. Commun.* **175**, 713–720 (2006).
28. A. O. Lyakhov, A. R. Oganov, H. T. Stokes, Q. Zhu, New developments in evolutionary structure prediction algorithm USPEX. *Comput. Phys. Commun.* **184**, 1172–1182 (2013).
29. L. Monacelli *et al.*, The stochastic self-consistent harmonic approximation: Calculating vibrational properties of materials with full quantum and anharmonic effects. *J. Phys.: Condens. Matter* **33**, 363001 (2021).
30. L. Monacelli, I. Errea, M. Calandra, F. Mauri, Pressure and stress tensor of complex anharmonic crystals within the stochastic self-consistent harmonic approximation. *Phys. Rev. B* **98**, 024106 (2018).
31. S. Klotz *et al.*, Bulk moduli and equations of state of ice VII and ice VIII. *Phys. Rev. B* **95**, 174111 (2017).
32. P. Loubeyre *et al.*, X-ray diffraction and equation of state of hydrogen at megabar pressures. *Nature* **383**, 702–704 (1996).
33. T. A. Strobel, M. Somayazulu, R. J. Hemley, Phase behavior of $H_2 + H_2O$ at high pressures and low temperatures *J. Phys. Chem. C* **115**, 4898–4903 (2011).
34. R. T. Howie, C. L. Guillaume, T. Scheler, A. F. Goncharov, E. Gregoryanz, Mixed molecular and atomic phase of dense hydrogen. *Phys. Rev. Lett.* **108**, 125501 (2012).
35. S. Schaack *et al.*, Orientational ordering, locking-in, and distortion of CH_4 molecules in methane hydrate III under high pressure. *J. Phys. Chem. C* **122**, 11159–11166 (2018).
36. S. Schaack *et al.*, Observation of methane filled hexagonal ice stable up to 150 GPa. *Proc. Natl. Acad. Sci. U.S.A.* **116**, 16204–16209 (2019).
37. J. S. Gardner, M. J. P. Gingras, J. E. Greedan, Magnetic pyrochlore oxides. *Rev. Mod. Phys.* **82**, 53 (2010).
38. H. Kadobayashi *et al.*, Structural evolution of methane hydrate under pressures up to 134 GPa. *J. Chem. Phys.* **152**, 194308 (2020).
39. N. Pantha, N. P. Adikhari, S. Scandolo, Decomposition of methane hydrates at high pressure: A density-functional theory study. *High Press. Res.* **35**, 231–238 (2015).
40. L. Sun *et al.*, X-ray diffraction studies and equation of state of methane at 202 GPa. *Chem. Phys. Lett.* **473**, 72–74 (2009).
41. H. Hirai, T. Tanaka, T. Kawamura, Y. Yamamoto, T. Yagi, Structural changes in gas hydrates and existence of a filled ice structure of methane hydrate above 40 GPa. *J. Phys. Chem. Solids* **65**, 1555–1559 (2004).
42. H. Hirai *et al.*, Phase changes of CO_2 hydrate under high pressure and low temperature. *J. Chem. Phys.* **133**, 124511 (2010).
43. X. Zhang *et al.*, Immiscibility in N_2–H_2O solids up to 140 GPa. *J. Chem. Phys.* **154**, 234505 (2021).
44. U. Ranieri *et al.*, Quantum dynamics of H_2 and D_2 confined in hydrate structures as a function of pressure and temperature. *J. Phys. Chem. C* **123**, 1888–1903 (2019).
45. Y. Fei *et al.*, Toward an internally consistent pressure scale. *Proc. Natl. Acad. Sci. U.S.A.* **104**, 9182–9186 (2007).
46. G. Shen *et al.*, Toward an international practical pressure scale: A proposal for an IPPS ruby gauge (IPPS-Ruby2020). *High Pres. Res.* **40**, 299–314 (2020).
47. Y. Akahama, H. Kawamura, Pressure calibration of diamond anvil Raman gauge to 310 GPa. *J. Appl. Phys.* **100**, 043516 (2006).
48. G. Kresse, J. Furthmüller, Efficient iterative schemes for ab initio total-energy calculations using a plane-wave basis set. *Phys. Rev. B* **54**, 11169–11186 (1996).
49. G. Kresse, D. Joubert, From ultrasoft pseudopotentials to the projector augmented-wave method. *Phys. Rev. B* **59**, 1758–1775 (1999).
50. P. Giannozzi *et al.*, QUANTUM ESPRESSO: A modular and open-source software project for quantum simulation of materials. *J. Phys.: Condens. Matter* **21**, 395502 (2009).
51. P. Giannozzi *et al.*, Advanced capabilities for materials modelling with quantum espresso. *J. Phys.: Condens. Matter* **29**, 465901 (2017).
52. D. R. Hamann, Optimized norm-conserving Vanderbilt pseudopotentials. *Phys. Rev. B* **88**, 085117 (2017).
53. G. Graziano, J. Klimeš, F. Fernandez-Alonso, A. Michaelides, Improved description of soft layered materials with van der Waals density functional theory. *J. Phys.: Condens. Matter* **24**, 424216 (2012).
54. T. Thonhauser *et al.*, Van der Waals density functional: Self-consistent potential and the nature of the van der Waals bond. *Phys. Rev. B* **76**, 125112 (2007).
55. R. Sabatini, E. Küçükbenli, B. Kolb, T. Thonhauser, S. de Gironcoli, Structural evolution of amino acid crystals under stress from a non-empirical density functional. *J. Phys.: Condens. Matter* **24**, 424209 (2012).

56. C. Pickard, R. Needs, Structure of phase III of solid hydrogen. *Nat. Phys.* **3**, 473–476 (2007).
57. L. Monacelli, I. Errea, M. Calandra, F. Mauri, Black metal hydrogen above 360 GPa driven by proton quantum fluctuations. *Nat. Phys.* **17**, 63–67 (2020).
58. L. Monacelli, M. Casula, K. Nakano, S. Sorella, F. Mauri, Quantum phase diagram of high-pressure hydrogen. *Nat. Phys.* **19**, 845–850 (2023).
59. L. Monacelli, F. Mauri, Time-dependent self-consistent harmonic approximation: Anharmonic nuclear quantum dynamics and time correlation functions. *Phys. Rev. B* **103**, 104305 (2021).
60. A. Siciliano, L. Monacelli, G. Caldarelli, F. Mauri, Wigner Gaussian dynamics: Simulating the anharmonic and quantum ionic motion. *Phys. Rev. B* **107**, 174307 (2023).